Materials & Design 224 (2022) 111405

Contents lists available at ScienceDirect

Materials & Design

journal homepage: www.elsevier.com/locate/matdes

Designing polyacrylic acid capped luminescent rare earth core–shell nanoparticles for simultaneous Cu(II) and temperature sensing

Yurong Luo [a], Hao Li [a], Muzhi Cai [a,*], Yuan Liu [b], Liang Chen [a], Shiqing Xu [a], Gongxun Bai [a,*]

[a] Key Laboratory of Rare Earth Optoelectronic Materials and Devices of Zhejiang Province, College of Optical and Electronic Technology, China Jiliang University, Hangzhou 310018, China
[b] Department of Applied Physics, The Hong Kong Polytechnic University, Hung Hom, Kowloon, Hong Kong SAR, China

HIGHLIGHTS

- Rare earth core–shell nanoparticles are designed and constructed for detecting Cu^{2+} and temperature.
- Förster resonance energy transfer based on rare earth nanoparticles is studied for Cu^{2+} sensing.
- The rare earth core–shell nanoparticles concurrently exhibit high sensitivity and superior selectivity.
- The relative sensitivity of rare earth core–shell nanoparticles reaches 1.23% K^{-1} for temperature sensing.

GRAPHICAL ABSTRACT

Rare earth core–shell nanoparticles are designed and constructed for detecting Cu^{2+} and temperature.

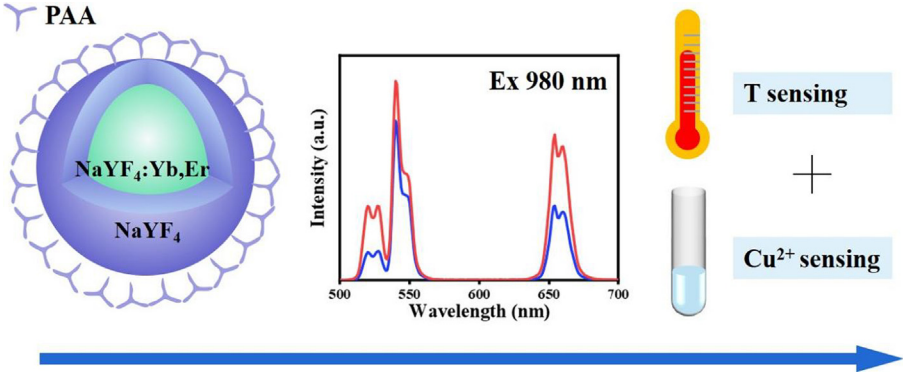

ARTICLE INFO

Article history:
Received 26 September 2022
Revised 13 October 2022
Accepted 20 November 2022
Available online 21 November 2022

Keywords:
Yb3+/Er3+ codoping
Cu2+ detection
Temperature sensing

ABSTRACT

Cu^{2+} is an essential trace element for humans and animals, and the precise detection of Cu^{2+} can help diagnose many diseases. However, the current Cu^{2+} detection technology still needs to be improved in terms of the biocompatibility of the material, the penetration of the excitation source, and the detection limit. In this paper, the polyacrylic acid (PAA) capped $NaYF_4$:Yb^{3+}/Er^{3+}@$NaYF_4$ core–shell nanoparticles (NPs) with a particle size of about 22.5 nm is proposed. Under the excitation of 980 nm with strong penetration, the Cu^{2+} concentration can be detected by the emission intensity of NPs at 520 nm, and the detection limit is 0.018 μM. In addition, this material can also perform temperature detection within 296–373 K with a relative sensitivity of 1.23 % K^{-1}. Therefore, this NPs is a promising multifunctional material that can detect temperature and Cu^{2+} concentration.

1. Introduction

Cu^{2+} widely exists in natural water and wastewater and is a trace element necessary for humans and most animals [1–3]. For example, neurotransmitters, synapses, hippocampus, and cerebellum contain Cu^{2+}, and the formation of melanin and the operation of some enzymes are also inseparable from Cu^{2+} [4–6]. Low levels of copper in the human body will lead to slow growth, anemia, and other symptoms, while high levels will affect the nerves, liver, cardiovascular, and kidneys [7–9]. Therefore, it is an essential requirement for further diagnosis that detects the content of copper ions

* Corresponding authors.
E-mail addresses: caimuzhi@cjlu.edu.cn (M. Cai), baigx@cjlu.edu.cn (G. Bai).

https://doi.org/10.1016/j.matdes.2022.111405
0264-1275/

in organisms and living water precisely [10,11]. There are many detection methods, such as atomic absorption spectrometry, inductively coupled plasma mass spectrometry, colorimetry, voltammetry, etc. [12–16]. However, they have their limitations, such as being unsuitable for biological applications, high detection limits, and low sensitivity [17,18].

Using optical probes to detect Cu^{2+} is a promising way because of a series of advantages like high response speed, low detection limit, high sensitivity, and low cost [19–21]. Commonly used probes for detecting Cu^{2+} include rhodamine B derivatives, coumarin derivatives, and gold NPs [22–24]. In recent years, rare earth-doped NPs have become commonly used as biosensing probes due to their sizeable anti-Stokes shift, long fluorescence lifetime, good biocompatibility, and high physicochemical stability [25–27]. Typically, in NPs based sensors, the NPs serve as energy donors, and the family of rhodamine B act as energy acceptors in the Förster resonance energy transfer (FRET) based Cu^{2+} detection. However, these sensors exhibit low emission when dispersed in water[9]. Recently, the sensor based on another FRET architecture that the NPs are still employed as energy donors while Cu^{2+} ions act as acceptors was proposed. For example, with Cu^{2+}, the carboxylate group of PAA can bind selectively to the Cu^{2+} ions owing to the electrostatic interaction between Cu^{2+} and carboxylate anion of PAA, forming copper carboxylate complex to quench the NPs fluorescence [1,9,18].

On the other hand, a multifunctional biosensing probe that can accomplish two tasks at once is desperately needed. Non-destructive temperature detection of the living organism is required in biological applications. In recent years, the temperature measurement method based on the fluorescence intensity ratio technology of rare earth doped nanoparticle materials has great application prospects in temperature detection due to its advantages of fast response speed, high sensitivity, and little influence by external conditions [28–31]. The doping of Yb^{3+} makes the material can be excited by the near-infrared 980 nm laser, which has the advantages of strong penetration in biological tissues and weak bio autoluminescence. Yb^{3+}/Er^{3+} codoped materials have become a research hotspot for thermometric materials due to their high luminous efficiency and wide temperature measurement range [32–34]. $NaYF_4$-basal core–shell material has the characteristics of a large specific surface area, low phonon energy, non-toxicity, high physical and chemical stability, can flexibly modify the surface, and can be combined with fluorescent probes, widely used in optical sensors. There have been many reports of biological temperature sensing using $NaYF_4$:Er^{3+}/Yb^{3+}, and the principle is that under the excitation of 980 nm, the ratio of the luminous intensity of the thermally coupled energy level pair ($^2H_{11/2}$ and $^4S_{3/2}$) of Er^{3+} ions changes regularly with temperature [35,36]. Meanwhile, as Cu^{2+} detection probes, Yb^{3+}/Er^{3+} codoped $NaYF_4$ NPs have also received wide attention because of their high Cu^{2+} detection limits [9,18,25].

In this paper, core–shell NPs with Yb^{3+}/Er^{3+}-doped $NaYF_4$ as the core layer and pure $NaYF_4$ as the shell layer were synthesized by co-precipitation method. The average particle size of the NPs is 22.5 nm, the thickness of the shell layer is 2.5 nm, and the NPs are capped by PAA. The optimal doping concentration of Er^{3+} was explored, and the X-ray diffraction (XRD), Transmission electron microscopy (TEM), and Fourier-transform infrared spectroscopy (FTIR) were used to characterize the material. Under excitation at 980 nm, the NPs can selectively detect Cu^{2+} with a superior detection limit. In addition, the fluorescence intensity ratio of 520 and 540 nm of the material can be used for temperature measurement, and it exhibits good temperature sensing properties within 296–373 K. Therefore, this core–shell NPs can be used as a multifunctional material integrating temperature sensing and Cu^{2+} detection, and has application prospects in biological, industrial and other fields.

2. Experimental

2.1. Materials

All chemicals below were used as received without further purification. Ytterbium acetate hydrate ($Yb(Ac)_3{\cdot}xH_2O$, 99.9 %), erbium acetate hydrate ($Er(Ac)_3{\cdot}xH_2O$, 99.9 %), yttrium acetate hydrate ($Y(Ac)_3{\cdot}xH_2O$, 99.9 %), oleic acid (OA, 90 %), 1-octadecene (ODE, 90 %) and poly acrylic acid (PAA) were obtained from Sigma Aldrich Company. Sodium hydroxide (NaOH, 96.0 %) and ammonium fluoride (NH_4F, 98 %) are supplied by Aladdin Industrial Corporation. Methanol (CH_3OH, 99.5 %), absolute ethanol (C_2H_6O, 99.7 %) and cyclohexane (C_6H_{12}, 99.5 %) were purchased from Sinopharm Chemical Reagent Company.

2.2. Preparation of $NaYF_4$:Yb^{3+}/Er^{3+} core NPs

$Y(Ac)_3{\cdot}xH_2O$ (0.78 mmol), $Yb(Ac)_3{\cdot}xH_2O$ (0.2 mmol), $Er(Ac)_3{\cdot}xH_2O$ (0.02 mmol), OA (6 mL) and ODE (14 mL) was added into a three-necked flask. After draining at 100 °C for 30 min, the mixture was kept at 150 °C for 30 min to obtain orange-yellow solution. After the solution was cooled to room temperature, methanol solution of NaOH (2 mmol) and methanol solution of NH_4F (1 mmol) were added dropwise in turn. Thereafter, keep the solution temperature at 80 °C for 30 min to remove methanol. Then rapidly raise the temperature to 290 °C for 2 h under nitrogen. After cooling to room temperature, the resultants were washed with cyclohexane-ethanol (1:1) and redissolved in 4 mL cyclohexane.

2.3. Preparation of $NaYF_4$:Yb^{3+}/Er^{3+}@$NaYF_4$ core–shell NPs

$Y(Ac)_3{\cdot}xH_2O$ (1 mmol) was mixed with OA (6 mL) and ODE (14 mL) in a three-necked bottle. The mixture was drained at 100 °C, and then kept at 150 °C for 30 min. After cooling to room temperature, 4 mL of the prepared cyclohexane solution of core NPs was added, and then cyclohexane was discharged at 70 °C. The solution was cooled to room temperature again, methanol solution of NaOH (2 mmol) and NH_4F (1 mmol) was added, and methanol was then discharged at 80 °C. Finally, the solution was rapidly heated to 290 °C for 2 h. After cooling, the core–shell NPs were obtained after centrifugation and washing.

2.4. Preparation of PAA capped NPs

The hydrophilic modification was performed with hydrochloric acid to wash off OA ligands on the surface of NPs. Then 0.1 mmol of PAA was added to the ligand-free NPs aqueous solution, and the pH was adjusted to 7 with NaOH. After stirring for 12 h, the PAA-capped NPs were obtained by washing with deionized water/ethanol (1:1).

2.5. Characterizations

In this work, the phase of $NaYF_4$:Yb^{3+}/Er^{3+}@$NaYF_4$ was identified by X-ray diffraction (XRD, D2 PHASER) with Cu-$K_{\alpha 1}$ irradiation, the 2θ range is from 10° to 80°. The morphology of NPs was observed by transmission electron microscope (TEM, FEI TECNAI G2 F20) and high-resolution transmission electron microscope (HR-TEM, JEM-2100F). The qualitative analysis of the NPs was performed by X-ray energy dispersive spectroscopy (EDS, SU8010), X-ray photoelectron spectroscopy (XPS, ESCALAB 250XI) and Fourier transform infrared spectroscopy (FTIR, BRUKER TENSOR 27). The emission spectra were obtained by a spectrometer (FL3-211-P), and the excitation source was a 980 nm laser.

3. Results and discussion

The phase analysis of the as-prepared NPs was carried out by XRD, as shown in Fig. 1a. The XRD spectrum is well matched to the standard card JCPDS#16–0334 of $NaYF_4$. There are diffraction peaks corresponding to (100), (110), (101), (201), and (211) crystal planes at 17.17, 30.02, 30.88, 43.65, and 53.83, respectively. It shows that the prepared $NaYF_4$:Yb^{3+}/Er^{3+}@$NaYF_4$ NPs have high crystallinity. The FTIR spectra can analyze the surface chemical bonds of OA and PAA-coated NPs [37]. As shown in Fig. 1b, the OA-coated NPs have peaks at 1418, 1563, 2850, and 2940 cm^{-1}, corresponding to the symmetric vibration of –COO, the asymmetric vibration of –COO, symmetric vibration of $–CH_2$, asymmetric vibration of $–CH_2$, respectively. The existence of these functional groups indicates that the surface ligand is OA. The PAA-NPs do not have a $–CH_2$ vibration peak, but at 1644 cm^{-1} a corresponding vibration peak for –COO, indicating that PAA successfully replaced OA.

Fig. 1c is the EDX spectrum of the prepared core–shell NPs, and the inset is its element map. The EDX spectrum demonstrates that this material contains F, Na, Y, Yb, and Er, which proves the successful incorporation of Yb/Er in the material, and the content of each element in the NPs is F > Y > Na > Yb > Er. The element map can also reflect that these five elements are uniformly distributed. In addition, XPS can also conduct a qualitative analysis of the material. Fig. 1d-e is the XPS survey spectrum of $NaYF_4$:Yb^{3+}/Er^{3+}@$NaYF_4$. It is clear that the material comprises Na, Y, F, Yb, and Er because the peak at 1071.08 eV belongs to Na 1 s, the peak at 685.08 eV corresponds to F 1 s, the peak at 186.28 eV refers to Yb 4d, the peak at 173.78 eV corresponds to Er 4d, and the peak at 185.48 eV relates to Y 3d.

The size and morphology of NPs have a crucial impact on luminescence, so morphology analysis is essential. TEM and HRTEM were used to analyze the morphology of the as-prepared NPs. Fig. 2a is the TEM image of the core NPs, from which it is apparent that the NPs are uniform in size and monodisperse, with approximately a regular hexagon. The particle size analysis in Fig. 2b reveals that the size of the core NPs is 16.9–18.1 nm, and the average size is about 17.5 nm. The HRTEM image of the core NPs (Fig. 2c) shows the crystal plane fringes of the core NPs with a d-spacing of 0.515 nm, corresponding to the (100) plane of the hexagonal phase $NaYF_4$. The inset further supports the fact that the core NPs have good crystallinity without obvious defects. The $NaYF_4$:Yb^{3+}/Er^{3+}@$NaYF_4$ are uniformly dispersed NPs, the majority of which are hexagonal and some of which are rectangular, as shown by the TEM images of the core–shell NPs (Fig. 2d). Fig. 2e is the particle size analysis of the core–shell NPs, which shows that the size distribution of the NPs is in the range of 21.7–23.3 nm, and the average diameter is about 22.5 nm. Therefore, it can be concluded that the thickness of the shell is about 2.5 nm, and the particle size distribution of the core NPs is narrower than core–shell NPs. Fig. 2f is the HRTEM image of the core–shell NPs, which can reflect the core–shell structure of the NPs, and can also indicate that the shape of the NPs is hexagonal.

The structure of the as-prepared core–shell NPs is shown in Fig. 3a. The core layer is Yb^{3+}/Er^{3+}-doped $NaYF_4$, and the outer layer is a protective undoped inert $NaYF_4$ shell with a modified PAA ligand. The NPs emit light under the excitation of a 980 nm laser. The luminescence mechanism is shown in Fig. 3b. The Yb^{3+} can receive the energy of the 980 nm laser and transition from the ground state energy level ($^4F_{7/2}$) to the excited state energy level ($^2F_{5/2}$). Because the energy range between theYb^{3+}:$^2F_{5/2}$ and the Er^{3+}: $^4I_{11/2}$, $^4F_{9/2}$, and $^4F_{7/2}$ is not more than 1000 nm, energy transfer can occur to make Er^{3+} in the excited state. In addition, Er^{3+} can also absorb the energy of the 980 nm pump source to generate ground-state transitions (GSA, $^4I_{15/2}$→$^2H_{11/2}$) and excited-state transitions (ESA, $^2H_{11/2}$→$^4F_{7/2}$ and $^4I_{13/2}$→$^4F_{9/2}$). After a series of non-radiative relaxations, the electrons accumulate at the $^2H_{11/2}$, $^4S_{3/2}$, and $^4F_{9/2}$, and then return to the $^4I_{15/2}$ by releasing photons, resulting in green emission at 520 and 540 nm, and red emission at 654 nm, respectively.

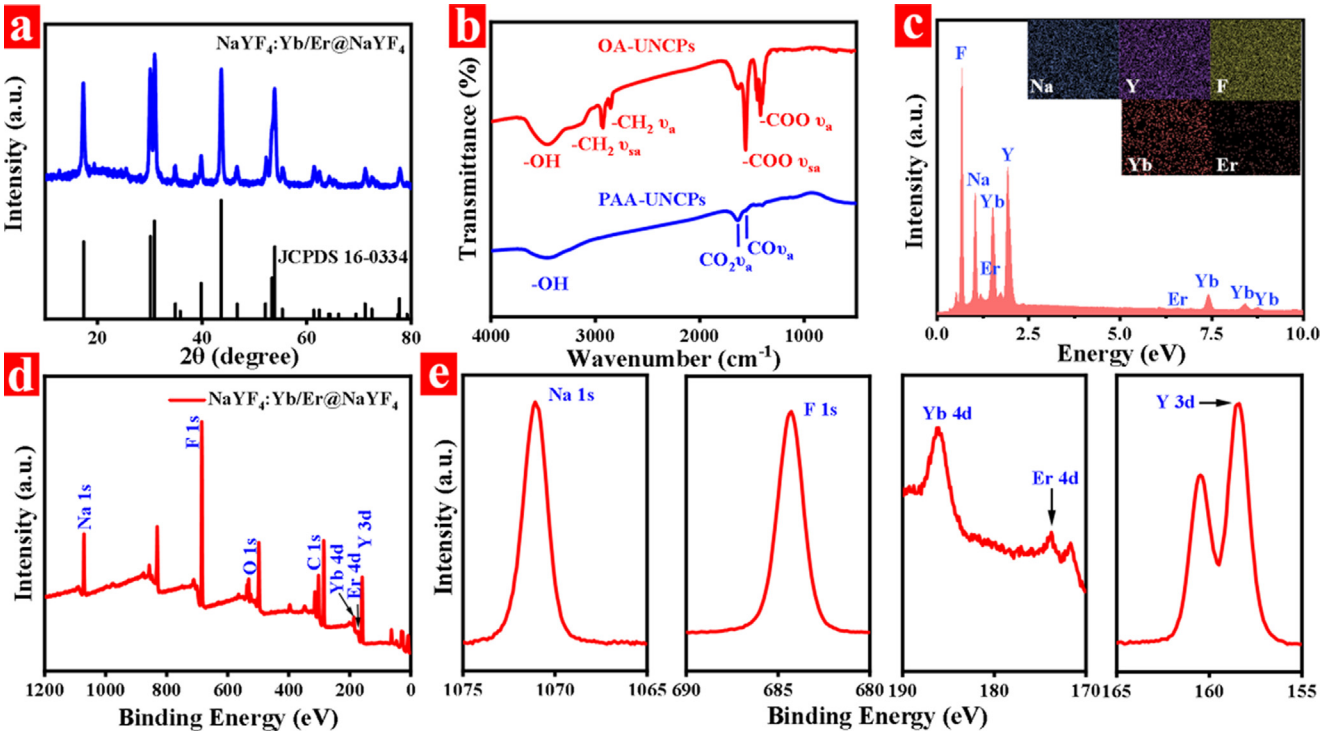

Fig. 1. (a) XRD patterns of the sample and $NaYF_4$ standard card, (b) FTIR spectra of OA and PAA coated NPs, (c) EDS and MAPPING characterization of the NPs, (d) XPS survey spectrum of $NaYF_4$:Yb^{3+}/Er^{3+}@$NaYF_4$, (e) XPS spectrum of Na 1 s, F 1 s, Yb 4d, Er 4d, Y 3d.

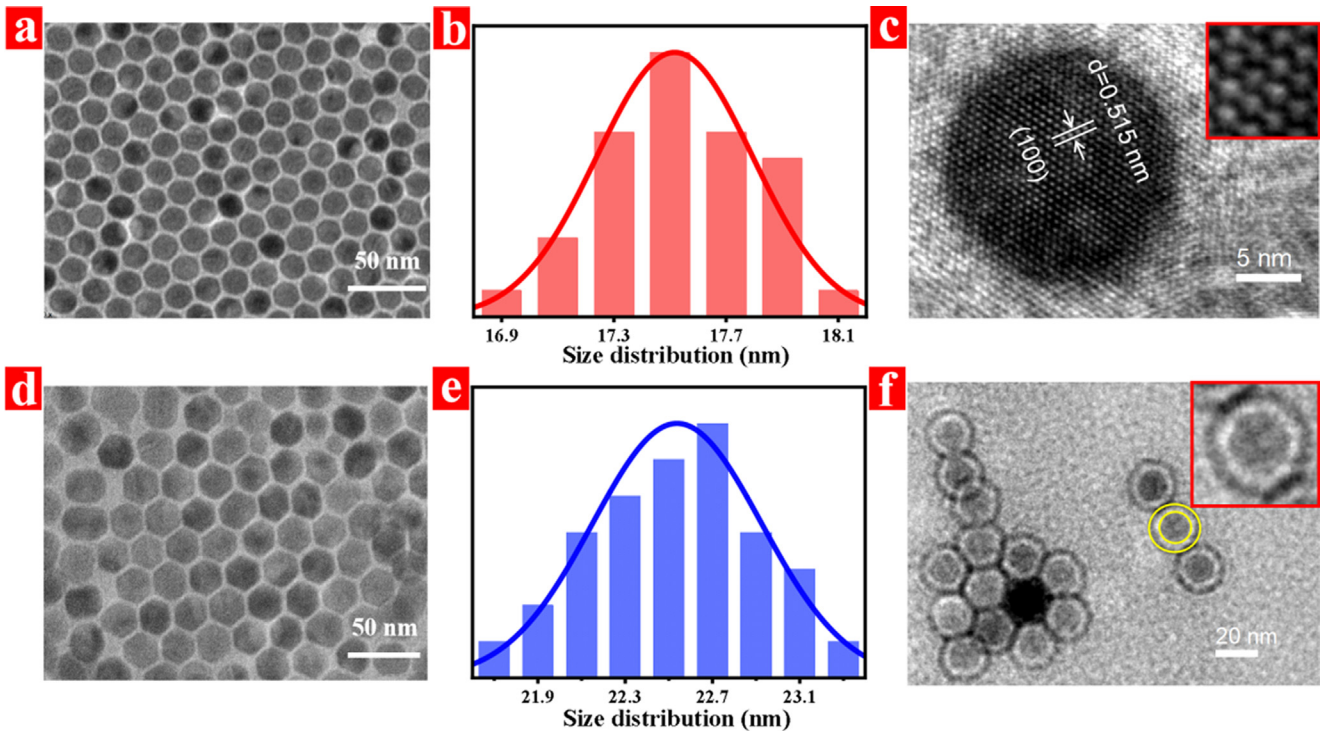

Fig. 2. TEM images (a), particle size distribution images (b) and HRTEM images (c) of $NaYF_4$:Yb^{3+}/E^{r3+} core NPs; TEM images (d) and particle size distribution images (e) and HRTEM images of $NaYF_4$:Yb^{3+}/Er^{3+}@$NaYF_4$ core–shell NPs.

To determine the optimal Er^{3+} doping concentration, we investigated the emission spectra of NPs with Yb^{3+} concentration of 20 % and Er^{3+} concentrations of 1 %, 2 %, 3 % and 4 %, as shown in Fig. 3c. When the Er^{3+} concentration is 2 %, the emission intensity reaches the highest, and as the Er^{3+} concentration continues to increase, the emission intensity decreases due to concentration quenching. Fig. 3d compares the luminescence intensities of core NPs and core–shell NPs. With the application of an inert shell layer, the core layer can be protected, and luminescence attenuation caused by external chemical and physical changes can be reduced. As a result, the luminescence intensity of the core–shell NPs is significantly enhanced, about 1.3 times that of the core NPs.

To investigate the upconversion emission of the $NaYF_4$:20 % Yb^{3+}/2%Er^{3+}@$NaYF_4$ NPs, the variation of luminescence intensity as affected by pump power was tested. As shown in Fig. 3e, the luminescence intensity of NPs is enhanced as the pump power increases. When the power density is 4.8 W/cm^2, the luminescence intensity at 520, 540, and 654 nm is enhanced to 29.9, 16.5, and 40.5 times that at 0.8 W/cm^2, respectively. There is a relationship between the luminous intensity (I) and the power density (P) as shown in Equation (1):

$$I \propto P^{n} \tag{1}$$

where n is the number of luminous photons. Therefore, taking the logarithm of luminous intensity and power density (as shown in Fig. 3f), the slope obtained by fitting is the number of pump photons. The n at 520, 540 and 654 nm is 1.93, 1.57 and 2.03, respectively, indicating that the transitions are all two-photon processes, which are the same as those reported [38].

There have been many studies on the detection of Cu^{2+} by PAA-modified NPs. These studies show that the detection of Cu^{2+} is based on the principle that when Cu^{2+} is present in the solution, the complex formed by Cu^{2+} and PAA accepts part of the energy from the NPs, resulting in the decay of the luminescence of the NPs. Fig. 4b shows the emission spectra of the materials under different Cu^{2+} concentrations. The concentration of Cu^{2+} in the solution was increased from 0 to 1.75 μM with an interval of 0.25 μM. With the increase of Cu^{2+} concentration, the luminescence intensity of NPs decreased and finally decreased by 70 %. The inset compares the luminescence photos of NPs before and after adding Cu^{2+}, which also reflects the decrease in luminescence brightness after adding Cu^{2+}. To explore the relationship between the concentration of Cu^{2+} and fluorescence quenching, we performed the Stern-Volmer plots shown in Fig. 4c, where I is the luminescence intensity at 540 nm after adding $CuCl_2$, I_0 is the initial luminescence intensity, and I_0/I-1 represents the luminescence decay efficiency. The detection limit (n_{min}) of Cu^{2+} can be obtained from Equation (2) [39,40]:

$$n_{min} = 3\sigma/S \tag{2}$$

where σ represents the standard deviation and S is the slope. In our research, the σ is 0.0072 and S is 1.23, so it can be concluded that the detection limit of Cu^{2+} detection based on this material is 0.018 μM, which is better than many reported materials [1,18,41]. To investigate the selectivity of NPs towards Cu^{2+}, the luminescence of NPs in other metal ion solutions was measured, as shown in Fig. 4d. In these metal ion solutions, the luminescence of NPs was attenuated, and the emission intensity was as follows: Fe^{3+} > K^+ > Ca^{2+} > Mn^{2+} > Zn^{2+} > Pb^{2+} > Co^{2+} ≫ Cu^{2+}. Only the luminescence in the Cu^{2+} solution can be significantly quenched, so the NPs synthesized in this paper can specifically detect Cu^{2+}.

At a pump power of 0.8 W/cm^2 of the used 980 nm laser, we measured the spectra of NPs in the range of 296–373 K with a temperature interval of 10 K. As shown in Fig. 5a, the NPs have emission bands at 509–534 nm, 534–563 nm, and 640–677 nm, corresponding to the $^2H_{11/2}$→$^4I_{15/2}$ transition, the $^4S_{3/2}$→$^4I_{15/2}$ transition, and the $^4F_{9/2}$→$^4I_{15/2}$ transition, respectively. And as the temperature increases, the emission intensity increases. It can also be seen in Fig. 5b that the main emission peaks have been enhanced to different degrees, and the peak at 520 nm has the most increase,

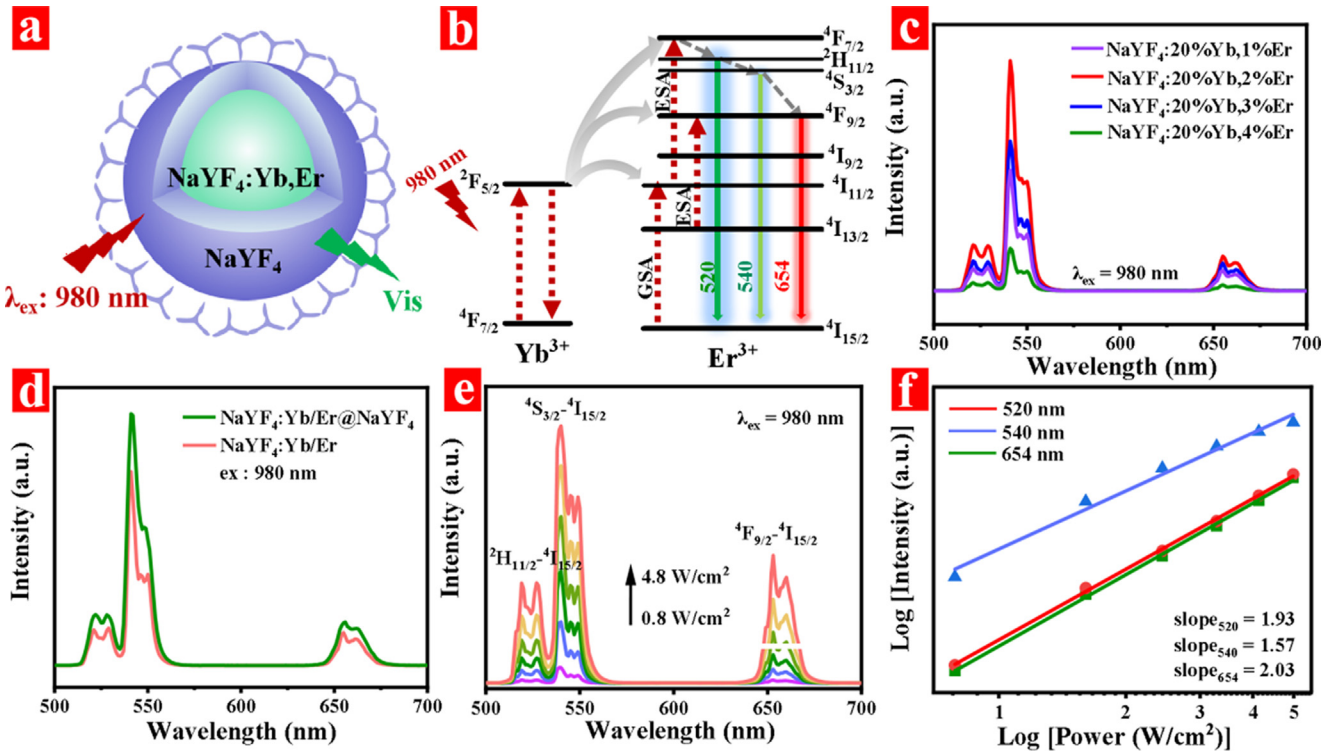

Fig. 3. Schematic diagram of luminescence (a) and energy level transition diagram (b) of core–shell NPs; (c) emission spectra of NPs with different Er^{3+} doping concentrations; (d) comparison of luminescence of core NPs and core–shell NPs; (e) power-dependent spectra of core–shell NPs; (f) logarithmic plot of pump power versus luminescence intensity.

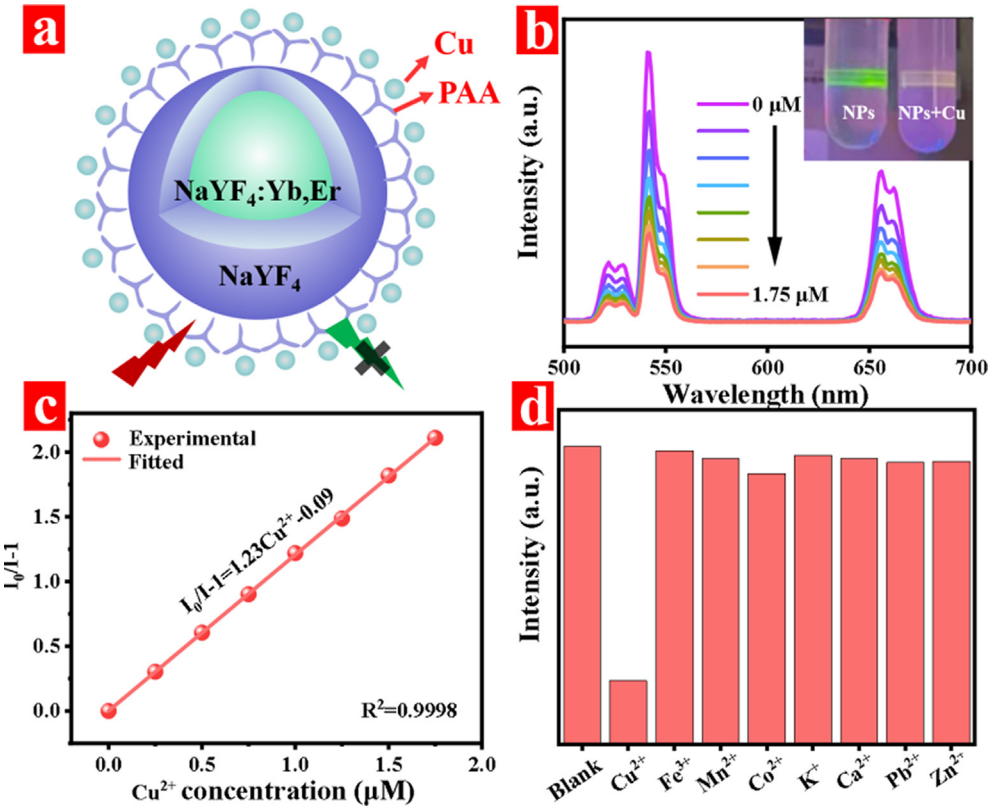

Fig. 4. (a) Schematic diagram of Cu^{2+} detection; (b) emission spectra of NPs in different Cu^{2+} concentrations; (c) Stern-Volmer plots of emission intensities (at 540 nm) and Cu^{2+} concentrations; (d) emission intensities of NPs in different metal ions.

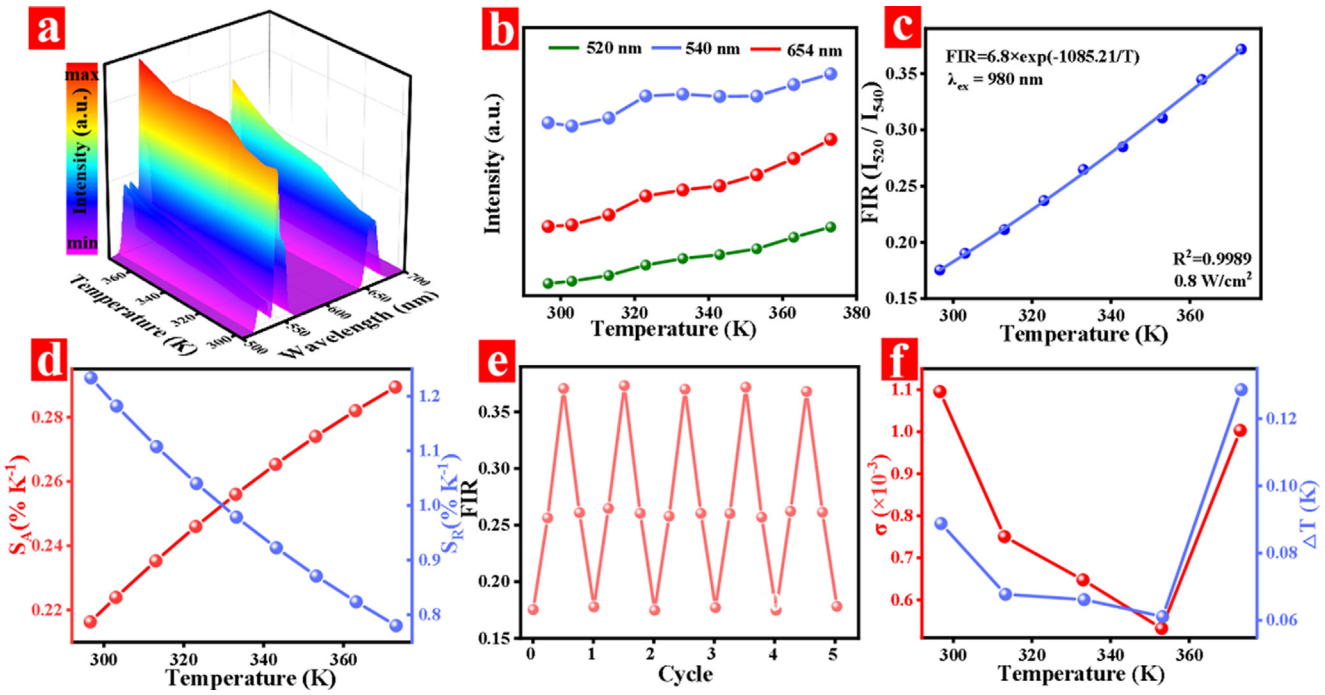

Fig. 5. (a) Temperature-variable spectra of NPs at 296–373 K; (b) emission intensity changes at 520, 540, and 654 nm; (c) FIR-temperature fitting curve; (d) relative and absolute sensitivity of temperature sensing; (e) FIR diagram of 5 repeated heating and cooling tests; (f) temperature uncertainty of temperature measurement.

with a 2.65-fold increase. The emission at 540 nm was increased by a factor of 1.25 with the slowest enhancement. $^2H_{11/2}$ and $^4S_{3/2}$ are used as the thermal coupling energy levels, and the fluorescence intensity ratio (FIR) technology is used to measure the temperature. The principle is shown in the following Equation (3) [42]:

$$FIR = \frac{I_2}{I_1} = \frac{g_2 A_2 h\nu_2}{g_1 A_1 h\nu_1} = C \exp\left(-\frac{\Delta E_{21}}{k_B T}\right) \tag{3}$$

where I_2&I_1, g_2&g_1, A_2&A_1, and ν_2&ν_1 represent the emission intensity, degeneracy, and spontaneous emission rate frequency of the thermal coupling energy levels, respectively. h is the Planck constant, C is a constant, $\triangle E_{21}$ is the energy range of the two energy levels, k_B is the Boltzmann constant, and T is the absolute temperature. Fig. 5c is the fitting curve of FIR-temperature for PAA-$NaYF_4$: Yb^{3+}/Er^{3+}@$NaYF_4$ NPs. It is obtained that C is 6.8, ΔE is 755 cm^{-1}. And R^2 is 0.9989, indicating that FIR correlates well with temperature.

Relative sensitivity (S_R) and absolute sensitivity (S_A) are important parameters to determine the temperature measurement performance of materials, and the analysis methods are shown in Equation (4) and Equation (5) [43]:

$$S_A = FIR \times \left(\frac{\Delta E_{21}}{k_B T^2}\right) \tag{4}$$

$$S_R = \frac{1}{FIR}\frac{dFIR}{dT} = \frac{\Delta E_{21}}{k_B T^2} \tag{5}$$

The S_A and S_R of the as-synthesized materials are given in Fig. 5d. The S_A ranges from 2.163 × 10^{-3} K^{-1} (296 K) to 2.894 × 10^{-3} K^{-1} (373 K). S_R ranged from 0.78 $\%K^{-1}$ (373 K) to 1.23 $\%K^{-1}$ (296 K). Among the optical temperature measurement materials doped with Yb^{3+}/Er^{3+}, the sensitivity of this material is above average [33,35]. Fig. 5e shows the FIR at 296, 333 and 373 K in 5 heating and cooling experiments. The deviation of each time is not large, indicating that the material has good repeatability. Another important parameter (temperature uncertainty, ΔT) that characterizes the temperature measurement performance can be obtained by processing the data of multiple experiments according to Equation (6):

$$\Delta T = \frac{\sigma}{S_R} \tag{6}$$

where σ denotes the standard deviation. As shown in Fig. 5f, and the σ is in the range of 0.53 × 10^{-3}-1.09 × 10^{-3}, the temperature uncertainty of this material is within 0.6–0.12 K, which is better than many reported materials [44,45]. Therefore, this material has excellent thermometric properties and has great prospects for biometric applications due to the good dispersion of PAA-modified NPs in water.

4. Conclusions

In conclusion, we prepared PAA-$NaYF_4$:20 $\%Yb^{3+}$/2%Er^{3+}@$NaYF_4$ core–shell NPs with a particle size of about 22.5 nm by the coprecipitation method. The materials were analyzed by XRD, XPS, EDS, FTIR, etc., which proved the successful incorporation of Yb^{3+}/Er^{3+} and the successful capping of the PAA on the surface of the NPs. Because of the specific binding of PAA and Cu^{2+}, the concentration of Cu^{2+} can be detected according to the change of the emission light at 520 nm of NPs, and the lowest detection limit can reach 0.018 μM. In addition, under the excitation of 980 nm, the synthesized material emits light at 509–563 nm and 645–676 nm. Utilizing luminescence at 520 and 540 nm, the NPs can perform temperature sensing detection within 296–373 K, and the sensitivity can reach 1.23 % K^{-1}. Therefore, the NPs can be a multifunctional material for temperature measurement and Cu^{2+} concentration detection, which has application prospects in Cu^{2+} detection and temperature sensing in biological, industrial, and other fields.

Data availability

No data was used for the research described in the article.

Declaration of Competing Interest

The authors declare that they have no known competing financial interests or personal relationships that could have appeared to influence the work reported in this paper.

Acknowledgments

This work was financed by the National Key Research and Development Project of China (2021YFB3502100), Zhejiang Provincial Natural Science Foundation of China (LZ21E020004), National Natural Science Foundation of China(6217032304), and Fundamental Research Funds for the Provincial Universities of Zhejiang.

References

[1] S. Sarkar, M. Chatti, V.H. Mahalingam, Luminescent Colloidal Eu^{3+}-Doped $KZnF_3$ Nanoparticles for the selective and sensitive detection of CuII ions, Chem-Eur. J. 20 (2014) 3311–3316, https://doi.org/10.1002/chem.201304697.

[2] S. Tottey, K.J. Waldron, S.J. Firbank, B. Reale, C. Bessant, K. Sato, T.R. Cheek, J. Gray, M.J. Banfield, C. Dennison, N.J. Robinson, Protein-folding location can regulate manganese-binding versus copper- or zinc-binding, Nature 455 (7216) (2008) 1138–1142.

[3] Z. Zhao, H. Chen, H. Zhang, L. Ma, Z. Wang, Polyacrylamide-phytic acidpolydopamine conducting porous hydrogel for rapid detection and removal of copper (II) ions, Biosens. Bioelectron. 91 (2017) 306–312, https://doi.org/10.1016/j.bios.2016.12.047.

[4] V.B. Kenche, I. Zawisza, C.L. Masters, W. Bal, K.J. Barnham, S.C. Drew, Mixed ligand Cu^{2+} complexes of a model therapeutic with alzheimer's amyloid-beta peptide and monoamine neurotransmitters, Inorg. Chem. 52 (2013) 4303–4318, https://doi.org/10.1021/ic302289r.

[5] K. Bossak-Ahmad, W. Bal, T. Fraczyk, S.C. Drew, Ternary Cu^{2+} complexes of human serum albumin and Glycyl-L-histidyl-L-lysine, Inorg. Chem. 60 (2021) 16927–16931, https://doi.org/10.1021/acs.inorgchem.1c03084.

[6] A.U. Rehman, S. Nazir, R. Irshad, K. Tahir, K.U. Rehman, R. Ul Islam, Z. Wahab, Toxicity of heavy metals in plants and animals and their uptake by magnetic iron oxide nanoparticles, J. Mol. Liq. 321 (2021), https://doi.org/10.1016/j.molliq.2020.114455 114455.

[7] J. Liu, X.L. Ren, X.W. Meng, Z. Fang, F.Q. Tang, Sensitive and selective detection of Hg^{2+} and Cu^{2+} ions by fluorescent Ag nanoclusters synthesized via a hydrothermal method, Nanoscale 5 (2013) 10022–10028, https://doi.org/10.1039/C3NR03329E.

[8] K.D. Fasae, A.O. Abolaji, T.R. Faloye, A.Y. Odunsi, B.O. Oyetayo, J.I. Enya, J.A. Rotimi, R.O. Akinyemi, A.J. Whitworth, M. Aschner, Metallobiology and therapeutic chelation of biometals (copper, zinc and iron) in Alzheimer's disease: Limitations, and current and future perspectives, J. Trace Elem. Med. Bio. 67 (2021), https://doi.org/10.1016/j.jtemb.2021.126779 126779.

[9] Y.B. Wang, W.X. Xu, L. Lei, L. Chen, R.G. Ye, S.Q. Xu, Photoluminescent $NaGdF_4$@$NaYF_4$:Ce/Tb inert-core/active-shell nanoparticles for selective and ultra-sensitive Cu^{2+} ions sensing, J. Lumin. 235 (2021), https://doi.org/10.1016/j.jlumin.2021.118024 118024.

[10] S.D. Richardson, S.Y. Kimura, Water analysis: emerging contaminants and current issues, Anal. Chem. 88 (2016) 546–582, https://doi.org/10.1021/acs.analchem.5b04493.

[11] C.X. Li, J.L. Liu, S. Alonso, F.Y. Li, Y. Zhang, Upconversion nanoparticles for sensitive and in-depth detection of Cu^{2+} ions, Nanoscale 4 (2012) 6065–6071, https://doi.org/10.1039/C2NR31570J.

[12] F. Tokay, S. Bağdat, Determination of Iron and Copper in Edible Oils by Flame Atomic Absorption Spectrometry After Liquid–Liquid Extraction, J Am Oil Chem Soc 92 (3) (2015) 317–322.

[13] E.B. Kim, M. Imran, E.H. Lee, M.S. Akhtar, S. Ameen, Multiple ions detection by field-effect transistor sensors based on ZnO@GO and ZnO@rGO nanomaterials: Application to trace detection of Cr (III) and Cu (II), Chemosphere 286 (2021), https://doi.org/10.1016/j.chemosphere.2021.131695 131695.

[14] P. Pohl, Determination of metal content in honey by atomic absorption and emission spectrometries, Trac-Trend, Anal. Chem. 28 (2009) 117–128, https://doi.org/10.1016/j.trac.2008.09.015.

[15] J.S. Becker, M.V. Zoriy, C. Pickhardt, N. Palomero-Gallagher, K. Zilles, Imaging of copper, zinc, and other elements in thin section of human brain samples (Hippocampus) by laser ablation inductively coupled plasma mass spectrometry, Anal. Chem. 77 (2005) 3208–3216, https://doi.org/10.1021/ac040184q.

[16] L.J. Bu, T.A. Gu, Y.X. Ma, C. Chen, Y.M. Tan, Q.J. Xie, S.Z. Yao, Enhanced cathodic preconcentration of As(0) at Au and Pt electrodes for anodic stripping voltammetry analysis of As(III) and As(V), J. Phys. Chem. C 119 (2015) 11400–11409, https://doi.org/10.1021/acs.jpcc.5b01435.

[17] Q.Y. Liu, J. Li, W.J. Yang, X.L. Zhang, C. Zhang, C. Labbe, X. Portier, F. Liu, J.L. Yao, B.D. Liu, Anal. Chim. Acta. 1100 (2020) 22–30, https://doi.org/10.1016/j.aca.2019.11.010.

[18] S.S. Su, Z.R. Mo, G.Z. Tan, H.L. Wen, X.D. Chen, A. Hakeem, PAA modified upconversion nanoparticles for highly selective and sensitive detection of Cu^{2+} ions, Front. Chem. 8 (2021), https://doi.org/10.3389/fchem.2020.619764 619764.

[19] M. Zhang, N.N. Wang, Z.H. Li, Recent advances in chromophore-assembled upconversion nanoprobes for chemo/biosensing, Trac-Trend. Anal. Chem. 151 (2022), https://doi.org/10.1016/j.trac.2022.116602 116602.

[20] Y. Fu, X.X. Pang, Z.Q. Wang, Q. Chai, F. Ye, A highly sensitive and selective fluorescent probe for determination of Cu (II) and application in live cell imaging, Spectrochim Acta. A. 208 (2018) 198–205, https://doi.org/10.1016/j.saa.2018.10.005.

[21] Q.Q. Wang, R. Hu, Z.Q. Fang, G.Y. Shi, S.Q. Zhang, M. Zhang, A multifunctional upconversion nanoparticles probe for Cu^{2+} sensing and pattern recognition of biothiols, Chinese Chem. Lett. 33 (2022) 3782–3786, https://doi.org/10.1016/j.cclet.2021.11.012.

[22] H. Hosseinjani-Pirdehi, N.O.A. Mahmoodi, A. Taheri, K.A.A. Asalemi, R. Esmaeili, Selective immediate detection of Cu^{2+} by a pH-sensitive rhodamine-based fluorescence probe in breast cancer cell-line, Spectrochim Acta. A. 229 (2020), https://doi.org/10.1016/j.saa.2019.117989 117989.

[23] X.H. Huang, L.J. Wang, X.J. Zhang, X.H. Yin, N. Bin, F.F. Zhong, Y.J. Liu, Q.Y. Cai, Dye-assembled nanocomposites for rapid upconversion luminescence sensing of Cu^{2+}, Sensor. Actuat. B-Chem. 248 (2017) 1–8, https://doi.org/10.1016/j.snb.2017.03.092.

[24] X.M. Yang, L. Yang, Y. Dou, S.S. Zhu, Synthesis of highly fluorescent lysine-stabilized Au nanoclusters for sensitive and selective detection of Cu^{2+} ion, J. Mater. Chem. C 1 (2013) 6748–6751, https://doi.org/10.1039/c3tc31398k.

[25] C.N. Sun, M. Gradzielski, Advances in fluorescence sensing enabled by lanthanide-doped upconversion nanophosphors, Adv. Colloid. Interfac. 300 (2022), https://doi.org/10.1016/j.cis.2021.102579 102579.

[26] Y. Liu, D.T. Tu, W. Zheng, L.Y. Lu, W.W. You, S.Y. Zhou, P. Huang, R.F. Li, X.Y. Chen, A strategy for accurate detection of glucose in human serum and whole blood based on an upconversion nanoparticles-polydopamine nanosystem, Nano Res. 11 (2018) 3164–3174, https://doi.org/10.1007/s12274-017-1721-1.

[27] C.N. Sun, M. Gradzielski, Upconversion-based nanosystems for fluorescence sensing of pH and H_2O_2, Nanoscale Adv. 3 (2021) 2538–2546, https://doi.org/10.1039/d0na01045f.

[28] L. Zheng, X.Y. Huang, J.P. Zhong, Z.J. Wang, X.N. Cheng, Upconversion luminescence and temperature sensing properties of $NaGd(WO_4)_2$:Yb^{3+}/Er^{3+}@SiO_2 core-shell nanoparticles, RSC Adv. 11 (2021) 3981–3989, https://doi.org/10.1039/d0ra10039k.

[29] M. Ding, J. Hou, Z. Cui, H. Gao, C. Lu, J. Xi, Z. Ji, D. Chen, Bundle-shaped β-$NaYF_4$ microrods: Hydrothermal synthesis, Gd-mediated downconversion luminescence and ratiometric temperature sensing, Ceram. Int. 44 (2018) 7930–7938, https://doi.org/10.1016/j.ceramint.2018.01.231.

[30] Y.R. Luo, Y. Liu, C.C. Wang, G.X. Bai, Y. Shen, Z. Jiang, S.Q. Xu, L. Chen, Near-infrared anti-Stokes luminescence from neodymium doped perovskite calcium titanate particles for optical temperature sensors, Sens. Actuat. A-Phys. 326 (2021), https://doi.org/10.1016/j.sna.2021.112741 112741.

[31] A. Kumar, J. Manam, Enhancement of dual-mode emission and temperature sensing performance in $Y_2Zr_2O_7$:Er^{3+} nano phosphor by incorporation of lithium ions, Ceram. Int. 48 (2022) 13615–13625, https://doi.org/10.1016/j.ceramint.2022.01.241.

[32] A.K. Soni, V.K. Rai, S. Kumar, Cooling in Er^{3+}:$BaMoO_4$ phosphor on codoping with Yb^{3+} for elevated temperature sensing, Sens. Actuat. B-Chem. 229 (2016) 476–482, https://doi.org/10.1016/j.snb.2016.01.144.

[33] Y. Li, L.N. Guo, T.S. Li, B.W. Yang, Up-conversion luminescence of $Lu_6O_5F_8$: 1%Er^{3+}/10%Yb^{3+}nanoparticles for temperature sensing and Cu^{2+} detection, Opt. Mater. 115 (2021), https://doi.org/10.1016/j.optmat.2021.111031 111031.

[34] G.J. Gao, D. Busko, S. Kauffmann-Weiss, A. Turshatov, I.A. Howard, B.S. Richards, Finely-tuned NIR-to-visible up-conversion in La_2O_3:Yb^{3+}, E^{r3}+ microcrystals with high quantum yield, J. Mater. Chem. C 5 (2017) 11010–11017, https://doi.org/10.1039/c6tc05322j.

[35] Y.R. Luo, L.B. Zhang, Y. Liu, E. Heydari, L. Chen, G.X. Bai, Designing dual-mode luminescence in Er^{3+} doped Y_2WO_6 microparticles for anticounterfeiting and temperature measurement, J. Am. Ceram. Soc. 105 (2022) 1375–1385, https://doi.org/10.1111/jace.18153.

[36] H.B. Xu, Y.B. Lian, Z.L. Lu, I. Kolesnikov, Y.J. Zhao, K. He, Z.W. Su, G.X. Bai, S.Q. Xu, Optical fiber temperature sensor of Er^{3+}/Yb^{3+} codoped $LaGaO_3$ microcrystals with high reliability and stability, J. Mater. Chem. C 10 (2022) 10660–10668, https://doi.org/10.1039/d2tc01462a.

[37] W. Kong, T.Y. Sun, B. Chen, X. Chen, F.J. Ai, X.Y. Zhu, M.Y. Li, W.J. Zhang, G.Y. Zhu, F. Wang, A general strategy for ligand exchange on upconversion nanoparticles, Inorg. Chem. 56 (2017) 872–877, https://doi.org/10.1021/acs.inorgchem.6b02479.

[38] A.F. Pereira, K.U. Kumar, W.F. Silva, W.Q. Santos, D. Jaque, C. Jacinto, Yb^{3+}/Tm^{3+} co-doped $NaNbO_3$ nanocrystals as three-photon-excited luminescent nanothermometers, Sens. Actuat. B-Chem. 213 (2015) 65–71, https://doi.org/10.1016/j.snb.2015.01.136.

[39] S. Sarkar, M. Chatti, V. Mahalingam, Highly luminescent colloidal Eu^{3+}-doped $KZnF_3$ nanoparticles for the selective and sensitive detection of Cu(II) ions, Chem. Eur. J. 20 (2014) 3311–3316, https://doi.org/10.1002/chem.201304697.

[40] X.H. Huang, L.J. Wang, X.J. Zhang, X.H. Yin, N. Bin, F.F. Zhong, Y.J. Liu, Q.Y. Cai, Dyeassembled nanocomposites for rapid upconversion luminescence sensing of Cu^{2+}, Sens. Actuat. B-Chem. 248 (2017) 1–8, https://doi.org/10.1016/j.snb.2017.03.092.

[41] M. Amjadi, J.L. Manzoori, T. Hallaj, N. Azizi, Sulfur and nitrogen co-doped carbon quantum dots as the chemiluminescence probe for detection of Cu^{2+}

ions, J. Lumin. 182 (2017) 246–251, https://doi.org/10.1016/j.jlumin.2016.10.021.
[42] H. Berthou, C.K. Jorgensen, Optical-fiber temperature sensor based on upconversion-excited fluorescence, Opt. Lett. 15 (1990) 1100–1102, https://doi.org/10.1364/OL.15.001100.
[43] S.A. Wade, S.F. Collins, G.W. Baxter, Fluorescence intensity ratio technique for optical fiber point temperature sensing, J. Appl. Phys. 94 (2003) 4743–4756, https://doi.org/10.1063/1.1606526.
[44] I.E. Kolesnikov, D.V. Mamonova, M.A. Kurochkin, V.A. Medvedev, G. Bai, T.Y. Ivanova, E.V. Borisova, E.Y. Kolesnikovc, Double-doped YVO4 nanoparticles as optical dual-center ratiometric thermometers, Phys. Chem. Chem. Phys. 24 (2022) 15349–15356, https://doi.org/10.1039/D2CP01543A.
[45] Y. Liu, G.X. Bai, E. Pan, Y.J. Hua, L. Chen, S.Q. Xu, Upconversion fluorescence property of Er^{3+}/Yb^{3+} codoped lanthanum titanate microcrystals for optical thermometry, J. Alloy. Compd. 822 (2020), https://doi.org/10.1016/j.jallcom.2019.153449 153449.